

Resolving the Ly α Forest

Greg L. Bryan¹

Princeton University Observatory, Princeton, NJ 08544

Marie Machacek

Department of Physics, Northeastern University, Boston, MA 02115

Peter Anninos

*Laboratory for Computational Astrophysics, National Center for Supercomputing Applications,
405 Mathews Ave., Urbana, IL 61801*

and

Michael L. Norman²

Astronomy Department, University of Illinois at Urbana-Champaign, Urbana, IL 61801

ABSTRACT

In this paper we critically examine predictions of the Ly α forest within the standard cold dark matter model. We show in particular that the width of these lines, typically measured by the b -parameter of a Voigt profile, is very sensitive to spatial resolution in numerical simulations and has previously been overestimated. The new result, which predicts a distribution with a median b of around 20 km/s at $z = 3$, is substantially below that observed. We examine a number of possible causes and argue that it is unlikely to be rectified by an increase in the temperature of the absorbing gas, but is instead telling us something about the distribution of matter on these scales. The shape of the b -parameter distribution agrees quite well with that observed, and the high-end tail is naturally produced by the filamentary nature of gravitational collapse in these models. We also examine the physical nature of the gas which is responsible for the forest, showing that for lines with neutral column densities below $N_{HI} \sim 10^{14} \text{ cm}^{-2}$ (for this model), the peculiar infall velocity is actually slower than the Hubble flow, while larger lines have, on average, turned around and collapsed.

Subject headings: cosmology: theory, intergalactic medium, methods: numerical, quasars: absorption lines

¹Lyman Spitzer Jr. Fellow

²also at National Center for Supercomputing Applications, Urbana IL 61801

1. Introduction

A physical picture of the Ly α forest in Cold Dark Matter (CDM) dominated cosmologies has recently emerged from numerical simulations (e.g. Cen et al. 1994; Zhang et al. 1995; Hernquist et al. 1996), and other approximation techniques (Bi 1993; Bi & Davidsen 1997; Hui, Gnedin & Zhang 1997; Gnedin & Hui 1998). In this context, the absorbers that give rise to low column density lines ($N_{HI} < 10^{15} \text{ cm}^{-2}$) at $z \sim 3$ are large, unvirialized objects with sizes of ~ 100 kpc, and low densities, comparable to the cosmic mean (Zhang et al. 1998). The width of the lines, as measured by the b parameter of a Voigt profile is set not only by thermal broadening or peculiar velocities, but by the Hubble expansion across their width (Weinberg et al. 1997). In such a situation, there is a monotonic relationship between baryonic density and optical depth which can be exploited to investigate the density distribution along the quasar lines of sight (e.g. Croft et al. 1998).

This explanation of the forest (for previous ideas along these directions, see also Bond, Szalay & Silk 1988 and Meiksin 1994), arising from gravitationally amplified primordial fluctuations, allows us to test various models of cosmological structure formation. This can be done, for example, by comparing the distribution of column densities (Gnedin 1998; Bond & Wadsley 1997; Machacek et al. 1998). These studies have found that the overall normalization of the distribution depends approximately on the parameter $(\Omega_b h)^2/\Gamma$ (there is also some dependence on gas temperature which varies with Ω_b). Here Γ is the HI ionization rate, h is the Hubble constant in units of 100 km/s/Mpc, and Ω_b is the ratio of the baryon density to the critical density required to close the universe. For a given model, this parameter is often set by requiring that the mean optical depth match that observed (Press et al. 1993; Zuo & Lu 1993; Rauch et al. 1997). The distribution of column densities is close to a power law and the slope provides much of the constraint, with the size of fluctuations on $\sim 200 - 500$ kpc scales being the key parameter (lower power causes a steeper slope; Gnedin 1998). Agreement seems to be found for a number of popular cosmological models. Another diagnostic is the distribution of b parameters found by fitting Voigt profiles to the spectra. This has been used to probe the reionization history (Haehnelt & Steinmetz 1997).

In this paper, we undertake a systematic evaluation of numerical uncertainties in simulations of the Lyman-alpha forest, and in doing so, explore the physical structure of the lines. We will show that the line structure can

be rather simply understood, but does require relatively high spatial resolution to model accurately, particularly for the fluctuations at or below the cosmic mean which give rise to the low end of the column density distribution. We cannot address either Lyman-limit or damped Lyman-alpha systems as they require more spatial resolution and physical processes than these simulations provide.

The paper is structured in the following way: in section 2, we examine the effect of resolution on various statistical measures of the forest and the gas that gives rise to it, looking first at distributions of density and temperature (section 2.2), and then at the properties of the lines fit to simulated spectra, in section 2.3. We analyze the physical nature of the lines in the next two sections (2.4 and 2.5), other non-parametric measures of the spectra (section 2.6), and the effect of our limited computational volume (section 2.7). Then we discuss these results and the corresponding observations in section 3.

While this paper was in the final stages of preparation, a preprint (Theuns et al. 1998) was circulated which examined some of the same issues, although with a different numerical method. Where there is overlap, our results are in agreement. In particular, they also find that the b -parameter distribution requires very high resolution.

2. The effect of spatial resolution

Most of the results for this section come from a set of three simulations in which we modeled the same region of space, but each time increasing the resolution by a factor of two. In generating the initial conditions, we keep constant not just the amplitudes but also the phases of the initial conditions (although, of course, higher resolution simulations contain more high-frequency power).

2.1. The simulations

The model is (nearly) the standard Cold Dark Matter (SCDM) model, with total and baryon density parameters $\Omega_0 = 1$ and $\Omega_b = 0.06$, respectively. The Hubble constant is $h = 0.5$, in units of 100 km/s/Mpc, and the matter fluctuation spectrum was normalized to $\sigma_8 = 0.7$, which measures the *rms* density fluctuations in a tophat sphere of $8h^{-1}$ Mpc. This normalization is considerably lower than the COBE measured CMB fluctuations would imply, however it is more in line with (although marginally higher than) the value indicated by the number density of large galaxy clusters (Viana & Liddle 1996; White, Efstathiou & Frenk 1993). We choose this model because it is a standard which we have simulated before (Zhang et al. 1997). The power spectrum is real-

istic enough to produce results which are characteristic of these kinds of hierarchical models, although certainly other parameters can be found which provide a better match to observations.

Our box size is $1.2h^{-1}$ Mpc, too small to include much of the large-scale power important to accurately determine the true distribution of column densities and b parameters, as we will show below (see also Wadsley & Bond 1997, Bond & Wadsley 1997). We adopt such a small volume in order to obtain the highest possible resolution for the lines we do resolve. In other words, we sacrifice the correct distribution of line widths and sizes under the assumption that the internal structure of a given line is not affected by the loss of large-wavelength power. We will show some supporting evidence for this with simulations of larger regions. Three different resolutions are computed, ranging from 32^3 to 128^3 cells, or cell sizes from $37.5h^{-1}$ kpc to $9.375h^{-1}$ kpc. In order to set this within the context of other simulations, we show the cell size of some other representative Eulerian Ly α simulations in Table 1, along with all the runs used in this paper. The first three lines are the resolution study runs that will be discussed in the next five sections, while the next five will be used to examine the effect of large-scale power (section 2.7). The gravitational softening length of these simulations is typically 1.5–2 cell widths. Also shown is the Hubble flow across Δx at $z = 3$, as well as the size of the box. We do not include the smoothed-particle hydrodynamics (SPH) simulations since their adaptive smoothing length makes a direct comparison difficult. However we note that the smoothing length of typical SPH simulations scales approximately as the interparticle spacing, which, for Hernquist et al. (1996), is $174 (\rho_b / \langle \rho_b \rangle)^{1/3} h^{-1}$ kpc, where $\langle \rho_b \rangle$ is the mean baryonic density. For the mean density at $z = 3$, this is a Hubble width of 34.8 km/s. The gravitational smoothing lengths of SPH simulations are typically much smaller ($10 h^{-1}$ kpc for Hernquist et al. 1996).

The simulation technique uses a particle-mesh algorithm to follow the dark matter and the piece-wise parabolic method to simulate the gas dynamics (described in detail in Bryan et al. 1995). Since non-equilibrium effects can be important, six species are followed (HI, HII, HeI, HeII, HeIII and the electron density) with a sub-stepped backward finite-difference technique (Anninos et al. 1997). We assume a spatially-constant radiation field computed from the observed QSO distribution (Haardt & Madau 1996 with an intrinsic spectral index of $\alpha = 1.5$), which reionizes the universe around $z \sim 6$ and peaks at $z \sim 2$.

As part of the analysis procedure, we generate spectra

along random lines of sight through the volume, including the effects of peculiar velocity and thermal broadening of the gas (Zhang et al. 1997). The spectra (the fitting is actually done with the optical depth distribution) are fit by Voigt-profiles to obtain column densities and Doppler widths for each line. To match observational samples, a minimum optical depth at line center ($\tau_{HI} = 0.05$) is required. The procedure is described in detail elsewhere (Zhang et al. 1997), but we point out here that it does not include noise or continuum-fitting. The spectra have a resolution of 1.2 km/s (regardless of the spatial resolution of the simulation), a value which is smaller than current observations. We use this technique since we are not interested in a detailed comparison to raw observations, but are more interested in exploring the physical nature of the lines. Still, we will show (by direct comparison) that the result of not including these observational effects is slight.

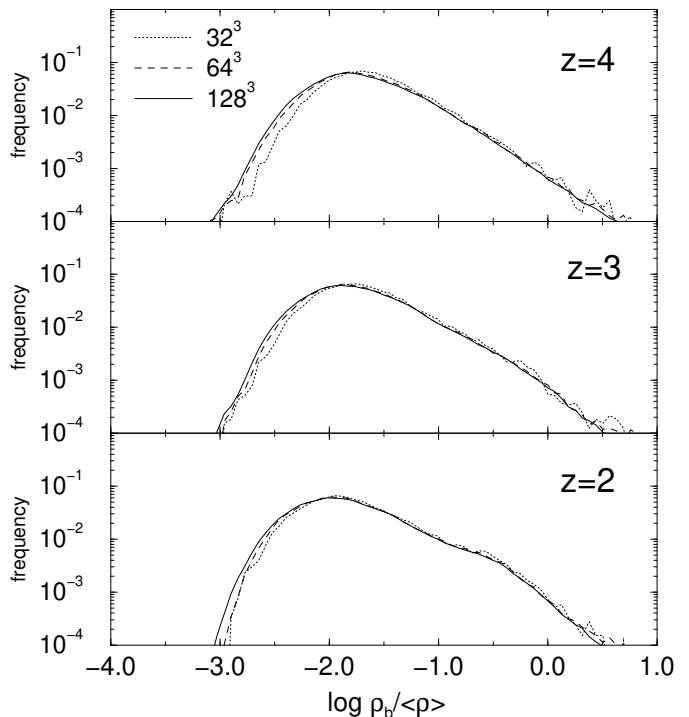


Fig. 1.— The distribution of baryon overdensity at three redshifts each for three simulations. The mean density in these units is $\log \Omega_b = -1.22$.

TABLE 1
SELECTED EULERIAN $\text{Ly}\alpha$ FOREST SIMULATIONS

| reference | Δx ($h^{-1}\text{kpc}$) | $H(z)\Delta x/(1+z)$ at $z=3$ (km/s) | L_{box} ($h^{-1}\text{Mpc}$) |
|----------------------------------|-----------------------------------|--------------------------------------|---|
| 32 ³ (this work) | 37.5 | 7.5 | 1.2 |
| 64 ³ (this work) | 18.9 | 3.8 | 1.2 |
| 128 ³ (this work) | 9.4 | 1.9 | 1.2 |
| L1.2 (this work) | 37.5 | 7.5 | 1.2 |
| L2.4 (this work) | 37.5 | 7.5 | 2.4 |
| L4.8 (this work) | 37.5 | 7.5 | 4.8 |
| L9.6 (this work) | 37.5 | 7.5 | 9.6 |
| L4.8HR (this work) | 18.9 | 3.8 | 4.8 |
| Zhang et al. 1998 top (sub) grid | 37.5 (9.4) | 7.5 (1.9) | 4.8 |
| Miralda-Escudé et al. 1996 L10 | 34.7 | 4.2 | 10 |
| Miralda-Escudé et al. 1996 L3 | 10.4 | 1.3 | 3 |

2.2. Physical properties

In Figures 1 and 2, we show the baryonic density and temperature distributions for the three simulations at three redshifts. The density distributions follow the usual approximately log-normal curve (although note the high-density tail), with the majority of the volume below the mean density. This pattern continues at lower redshifts as the voids deepen and the filaments and peaks grow. The difference between resolutions is relatively small, although there is a slight tendency for the higher resolution simulations to have more low-density cells, due both to their additional small-scale power as well as to the improved resolution of the small-scale features already present.

The temperature distribution can be described as three features (seen most clearly in the density-weighted distribution). The central one is a peak at slightly above 10^4 K, representing dense gas which has collapsed, shock heated and then cooled, generally by line-emission, to this temperature (below which emission processes for our assumed metal-free gas are inefficient). This virialized material is quite dense but occupies a small volume as can be seen by contrasting the volume and density weighted distributions. This means that, although they may be quite prominent in emission features (and indeed would possibly undergo star formation if such processes were included), most of the absorption lines, by number, come from low-density regions that occupy the majority of the volume.

The second feature shows up in these plots as a low-temperature shoulder which moves even further to the

left at lower redshift and is low-density gas which was originally heated to $\sim 15,000$ K by reionization occurring between $z=7$ and 6. It then adiabatically cools with the universal expansion and, because of the low HI fraction and low recombination rate, ionization heating is insufficient after $z \sim 5$ to keep this gas from cooling below 10^4 K. Most of it is below the mean baryonic density.

The third feature is a long, power-law profile of shock-heated material above 10^5 K that is too low-density to cool efficiently. It comes from the halos of clumps, filaments and, in some cases, sheets. The amount of such gas increases with time as longer waves go non-linear, although it is clear that the volume occupied by such gas is extremely small, and will not contribute significantly to the bulk of the $\text{Ly}\alpha$ forest. As we will demonstrate in section 2.7, the sharp cutoff at $T \sim 10^5\text{--}10^6$ K is due to the artificial lack of large-scale power.

The effect of resolution is again quite small. There are some differences in the high-temperature end, particularly when looking at the mass-weighted statistic, which is due to the improved resolution around small collapsed objects. More interestingly, from the standpoint of the forest, higher resolution systematically produces more low-temperature gas. Such a trend is expected from the change in the density distribution described above (lower density regions are cooler due to expansion cooling and reduced photo-ionization heating).

2.3. Line properties

We have seen that there are some, albeit slight, changes to the gross distribution functions of the physical vari-

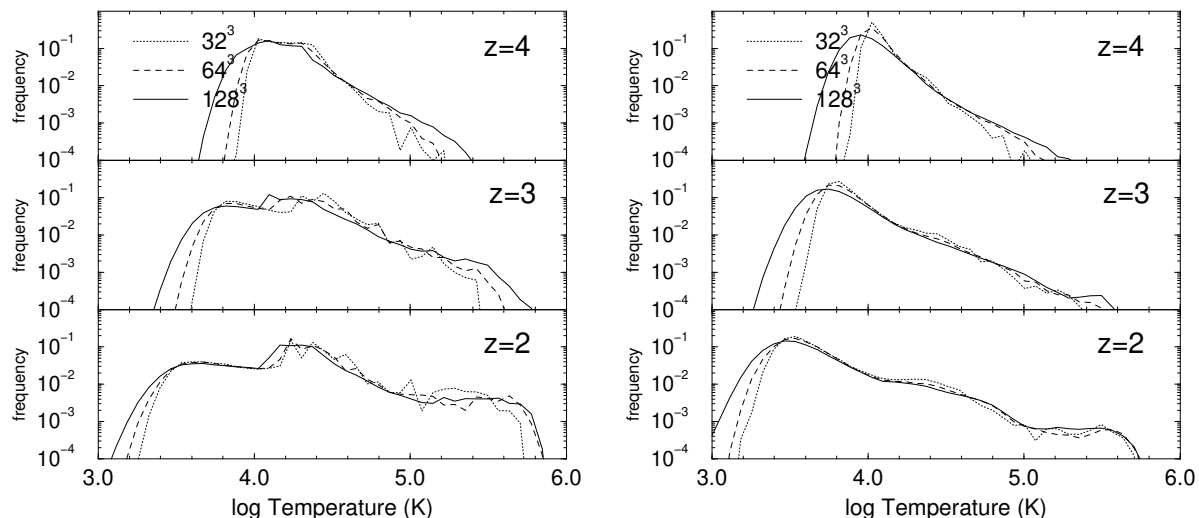


Fig. 2.— The distribution of density-weighted temperature (left panels) and volume-weighted temperature (right panels) at three redshifts each for three resolutions.

ables in the simulations. We ask here what change the resolution has on the observables of the Ly α forest. In Figure 3, we show the distribution of column densities of neutral hydrogen for our three different resolutions. Although there are fluctuations at the higher column density end due to shot noise from the small number of absorbers, the only systematic differences are at high redshift, for the lowest column densities, where observations are also uncertain. This arises because this redshift and column density range probes the smallest fluctuations present in the simulation (those which are around the Jean's length, a fact which will be discussed in more detail below). As the cell width goes down, these fluctuations become better resolved resulting in an increase in the number of these low column-density lines.

Otherwise, there is remarkable agreement, demonstrating the forgiving nature of the column density distribution. Roughly speaking, this is due to the fact that the column density of a given line is basically an integrated quantity and is not sensitive to the detailed shape of the gas profile. This also comes into play at the high column density end which comes from the dense, cooling knots (see also Zhang et al. 1998). At high resolutions these cores become smaller and denser but, remarkably, this does not appear to substantially affect the column density distribution because their cross-sections also decrease. Lines with column densities of around $10^{16.5}$ and higher suffer from significant self-shielding, a process we have not included in the simulations, so we do not go

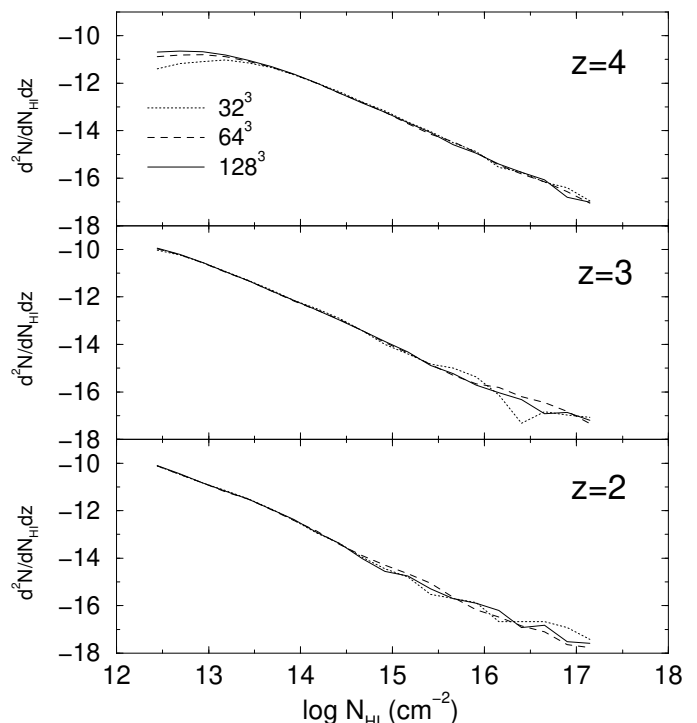


Fig. 3.— The distribution of neutral hydrogen column densities for three redshifts with three different resolutions, ranging from 32^3 cells (dotted line) in a $1.2h^{-1}$ Mpc box, to 128^3 cells (solid line).

beyond this point.

The second quantity typically used to parameterize a Voigt profile is the Doppler b parameter which measures the width of the line. Unlike the column density this parameter is sensitive to resolution, as Figure 4 demonstrates. We restrict ourselves to column densities greater than 10^{13} cm^{-2} and less than 10^{14} cm^{-2} , since this range is well-constrained observationally and does not suffer so much from selection effects due to the minimum optical depth cut mentioned earlier (the behaviour of lines with column densities outside of this range is quite similar).

The shape of the distribution may appear unfamiliar to those used to seeing this quantity plotted linearly, but the profile is much like that seen observationally. The mean, in contrast, particularly for the highest resolution case, is much smaller than observed, which is around 30 km/s (Hu et al. 1995; Kirkman & Tytler 1997; Kim et al. 1997). This figure is one of the main results of this paper, since it demonstrates that (1) previous simulations have

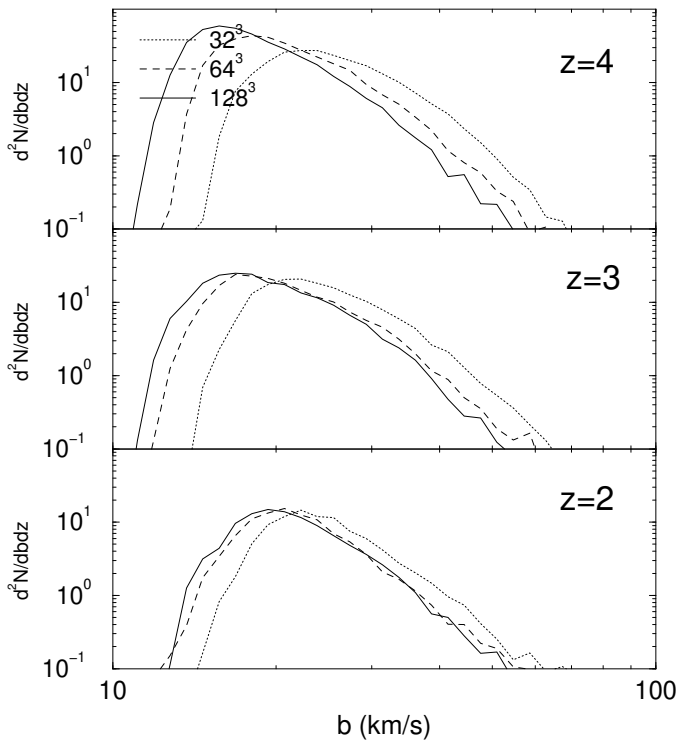


Fig. 4.— The distribution of Doppler b parameters (for lines with column densities $10^{13} < N_{HI} < 10^{14} \text{ cm}^{-2}$) for the same three redshifts and resolutions as in figure 3. Higher resolution simulations produce distributions shifted to smaller b .

over-estimated the line widths, and (2) this model, which has previously been shown to predict results (at least for the Ly α forest) in agreement with observations, is now discrepant. Since it is of some significance, we will spend much of the rest of the paper examining this point more closely.

The entire distribution tends to shift to the left as the resolution improves, which means that each line decreases by a constant fraction of its width. Since the shape is largely invariant (we will explore this point in more detail later), we can characterize the shift by the change in the median of the distribution. To show the trend more clearly, Figure 5 plots the median b against resolution. The drop at $z = 3$ is about 5 km/s going from a comoving cell size of $37.5 h^{-1} \text{ kpc}$ to our highest resolution at $9.375 h^{-1} \text{ kpc}$. The effect is clearly largest at high redshift, and shows signs of convergence by $z = 2$. We also note that for the highest resolution simulations, there is a clear trend of increasing b parameter with decreasing redshift, as observations also seem to indicate (Kim et al. 1997), although of course with much larger median b 's.

An important question that needs to be addressed is whether such low values are due to our rather idealized Voigt-profile fitting procedure. We test this possibility with the automated Voigt-profile fitting package AUTOVP (Davé et al. 1997), kindly provided to us by Romeel Davé. The spectra are smoothed to approximate the resolution of HIRES, and noise is added, both

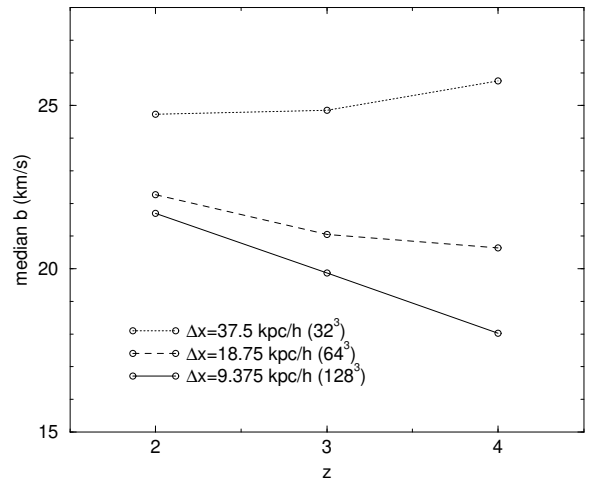


Fig. 5.— The median of the Doppler b distributions shown in Figure 4 as a function of redshift and resolution (for lines in the $N_{HI} = 10^{13} - 10^{14} \text{ cm}^{-2}$ range). Higher resolution simulations produce thinner lines.

a readout component and a Gaussian photon noise with a signal-to-noise ratio of 60. We fit one hundred of our $\Delta z = 0.1$ spectra for a relatively difficult case, the 128^3 simulation at $z = 3$, which exhibits many narrow lines. The result, shown in Figure 6, demonstrates that while there are some differences — which would probably be greater for lower signal-to-noise spectra — the basic outcome is unchanged. Indeed, this is unsurprising: the presence of metal lines in observed spectra proves that there is no intrinsic difficulty in fitting thin lines.

2.3.1. What causes b to decline with resolution?

The width of a particular line can be affected by the gas temperature, the peculiar velocity structure, and the density profile of the line. An increase in the temperature would increase the Doppler broadening; an expanding structure (or even one collapsing less quickly) can broaden the profile; finally the density distribution itself can give rise to such an effect, since a line that is physically wider will cover more of the Hubble flow.

In order to determine the cause of the decline seen in the previous section, we must look at the underlying gas distribution that gives rise to each line. In Figure 7 we plot the same line-of-sight for the three different resolutions at $z = 3$. There is rough correspondence between large features, however the details vary strongly, particu-

larly for the 32^3 run (compared to the others). Unfortunately, a comparison of this type is not particularly useful due to the chaotic nature of the non-linear evolution; slight differences in, say, the position of a clump can give rise to large discrepancies along a particular line of sight. Still, a number of broad conclusions can be drawn. The first is that the large-scale velocity and density structures are well followed, although in at least one case (around 200 km/s), the differences are surprising large. The two better-resolved simulations tend to track each other with satisfying fidelity. The second is that a qualitatively new feature appears to have arisen in the high-resolution temperature profiles — high amplitude fluctuations on the 20 km/s ($100 h^{-1}$ kpc) scale. We will return to this observation below.

While such anecdotal evidence is interesting, it is more useful to look at the mean behaviour of the lines. The difficulty in doing this is to associate a given flux decrement (line) with the range of cells which create it. Because of Doppler shifts due to peculiar velocities in the gas, there

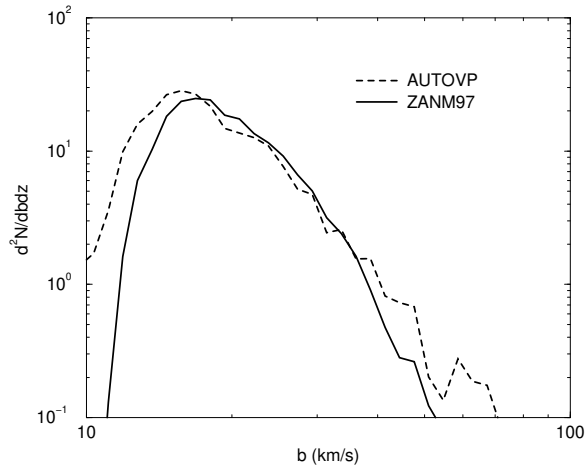


Fig. 6.— A comparison of the Doppler b distribution resulting from fitting with two different techniques, one without noise (Zhang et al. 1997, denoted ZANM97 in the figure) and one with noise (AUTOVP, kindly provided by Romeel Davé). The spectra are from the 128^3 simulation at $z = 3$.

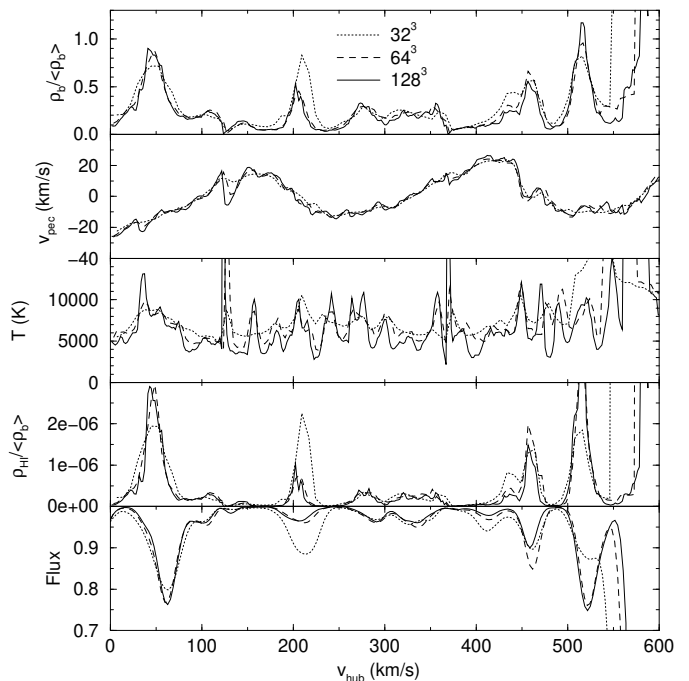


Fig. 7.— The profiles of various quantities resulting from the same line-of-sight taken through the three simulations at $z = 3$. The ordinate is the Hubble velocity corresponding to that cell (for baryonic density, temperature, velocity, and HI density) or the wavelength (converted to km/s) for the flux.

does not have to be a one-to-one correspondence. However, for the vast majority of lines, the correspondence is clear. Still, we need to remove the peculiar velocity contribution in order to do this association; fortunately, the bulk velocity component changes slowly, so this task is relatively straightforward.

For each line in the given range, we compute the average peculiar velocity \bar{v}_{pec} of the gas that gives rise to that line (i.e. for each gas parcel that contributes to a particular line, we include its peculiar velocity weighted by its contribution to the flux, and compute the mean of this quantity). This value is then used to correct from the observed line center (v_{line}) to our best estimate of the line center as measured by the Hubble velocity along the line-of-sight: $v_h = v_{line} - \bar{v}_{pec}$. Once this estimated center has been computed, it can be converted to a physical position along the LOS by inverting the Hubble law.

We then follow the LOS in both directions (positive and negative velocity) until a density minimum is encountered along each path. This section is extracted and used to compute the mean profiles shown in Figure 8 (in order to prevent small fluctuations from introducing small minima which would cause us to extract too small a section, we smooth the density while checking for minima). We discard lines that do not have a density maximum within 20 km/s of the estimated line center (about 5% of the total), since visual inspection of a sample of these showed them to fall on the wings of much larger lines. This entire procedure is, in fact, quite robust to small changes in the details.

Since the column density is a robust prediction, we extract those lines which lie within a small range of N_{HI} and plot the results in Figure 8. We first discuss the left hand column, which shows a resolution study for a large number of lines (drawn from 300 samples each of length $\Delta z = 0.1$) from the same three simulations discussed previously. Only lines in the range $N_{HI} = 10^{13.0} - 10^{13.1}$ are used. Although individual lines can differ in detail, these mean profiles are characteristic; to give an idea of the variation, the *rms* scatter in $\rho_b / \langle \rho_b \rangle$ is about 0.3.

Systematic resolution effects are visible in each quantity. The density profiles, both baryonic and dark, are narrower with higher resolution, although the largest changes are in the dark matter profile, while the baryons show a flatter central profile. The temperature profile is relatively unchanged, although it becomes somewhat narrower and features a central depression at high resolution. The peculiar velocity profile develops a kink in the central 20 km/s with cell sizes less than than $37.5 h^{-1}$ kpc.

This figure confirms (Weinberg et al. 1997) that a large part of the line-broadening is due to the Hubble flow across the line width, and that the peculiar velocities tend to narrow this width somewhat (although thermal Doppler broadening also contributes). We first address the effect of resolution, and then, in the next section, turn to what the figure can tell us more generally about the lines.

Plotting the physical quantities in this way allows us to directly answer the question posed earlier. Of the three possible causes for the decrease in the line width, the most significant is the density, which shows a clear decrease in width as the resolution improves. This is particularly true in the outskirts of the line, which contributes preferentially to the line thickness. This can be roughly quantified by the width of a Gaussian fit to the density profile (the Voigt profile for low-column density Ly α lines is well approximated by a Gaussian). Although it is approximately Gaussian in shape, it is impossible to fit both the inner and outer parts with the same parameters; however, using only the outer points (beyond ± 10 km/s), the fit width decreases by 25% in going from the 32^3 to the 128^3 simulation. The inner part shows a less dramatic 10% decline. These figures are comparable to the drop in the median b with resolution.

This plot also shows that the change in the peculiar velocity is not primarily responsible for increasing the line width, since the magnitude of the change is only around 1 km/s. The temperature also adds to the width somewhat, as the high resolution profile is narrower, so the gas temperature in the line edges is reduced. This reduces the Doppler broadening (which contributes a width of approximately $13 (T/10^4\text{K})^{1/2}$ km/s), but again only by about 1 km/s or so.

From this discussion, we can conclude that the primary reason for the shift in the b distribution is numerical thickening of the lines. This shows up most clearly in the density profile, but it also affects the temperature distribution.

2.4. The physical nature of the absorbers

These profiles also tell us a great deal about the physical nature of the absorbers. The velocity plot (still focusing on the left hand side of Figure 8) indicates that these lines are infalling in comoving coordinates, but the amplitude, which is less than the Hubble expansion, reveals that the objects are actually expanding in absolute coordinates. This means, that while the overdensity ($\rho_b / \langle \rho_b \rangle$) may be increasing slowly, the absolute density is dropping

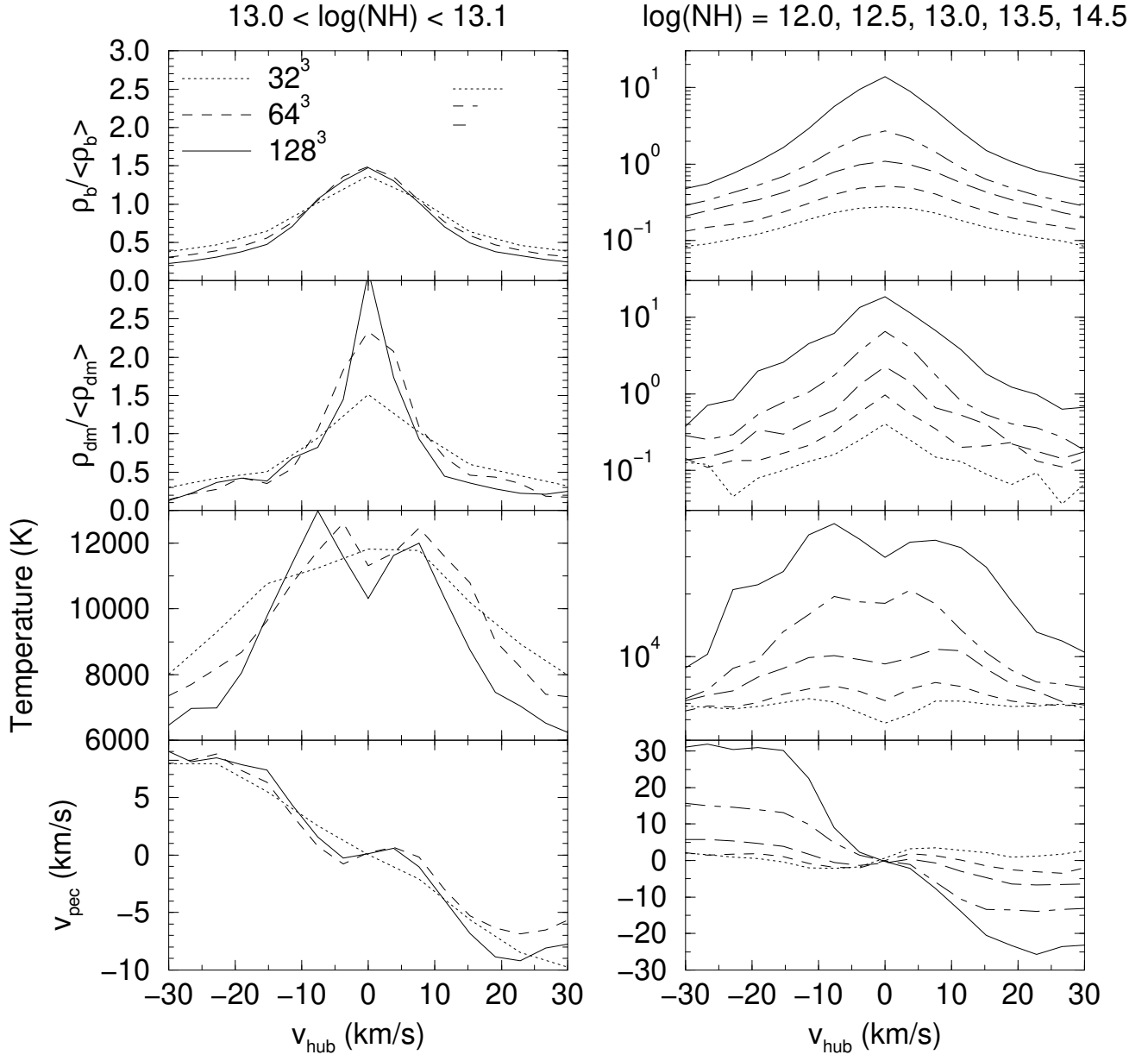


Fig. 8.— Mean profiles, at $z = 3$ of (from top to bottom) baryon overdensity, dark matter overdensity, temperature, and peculiar velocity projected along the line of sight. The left column shows results from three simulations with varying resolution for lines with neutral hydrogen column densities in the ranges $N_{HI} = 10^{13.0} - 10^{13.1} \text{ cm}^{-2}$. In the upper left panel, three lines show the cell size for each simulation. The right column shows the same quantities from the highest resolution simulation for a range of column densities. From top (solid) to bottom (dotted), the lines correspond to column densities in the ranges: $N_{HI} = 10^{12.0} - 10^{12.1}$, $10^{12.5} - 10^{12.6}$, $10^{13.0} - 10^{13.1}$, $10^{13.5} - 10^{13.6}$, and $10^{14.5} - 10^{14.7} \text{ cm}^{-2}$.

(at least for absorbers with this column density).

The temperature follows largely from the density profile: the recombination rate is larger at higher densities and so the photoionization heating is more effective. Lower densities have also undergone more expansion cooling. This dependence on density results in a polytropic equation of state (Hui & Gnedin 1997; see also Giroux & Shapiro 1996): $T \sim \rho^{0.5}$, by $z = 3$. The temperature contributes a width to the lines via Doppler broadening which is approximately $13 (T/10^4 \text{K})^{1/2} \text{ km/s}$, and so dominates the width only for lines which are intrinsically thin.

Finally, we turn to the details of the line center. The density profile shows a rounded top as opposed to the cuspy center of the dark matter. This is due to the effect of thermal pressure. Prior to reionization, the gas and dark matter profiles follow each other; however, once reionization occurs the gas temperature is raised everywhere to a nearly constant 15,000 K (the exact temperature depends somewhat on the assumed ionizing spectrum). The gas in the center of these objects, which are most likely to be sheets or filaments (e.g. Zhang et al. 1998), finds itself over-pressured and starts to expand. This (relative) expansion can be seen in the peculiar velocity profile as the kink mentioned previously, and also cools the gas, causing the central temperature depression.

On the right-hand side of Figure 8 are plotted mean profiles for a range of column densities from $N_{HI} = 10^{12}$ to $10^{14.5} \text{ cm}^{-2}$ (now using only the highest resolution simulation). Above this value there are too few lines, with too much diversity for a reasonable mean profile to be constructed. Other studies (Zhang et al. 1998; Cen & Simcoe 1997) have shown that the highest density absorbers ($\rho_b / \langle \rho_b \rangle \gtrsim 10$; $N_{HI} \gtrsim 10^{14}$ at $z = 3$ in this model) tend to be quasi-spherical, lying at the intersection of filaments, while progressively lower density absorbers occur in filaments and then sheets. We focus mostly on these latter two kinds of absorbers. We remind the reader that this correspondence between overdensity and column density depends not only on redshift, but also on a number of model-dependent factors, including Ω_b , h and the photoionization rate.

The density profiles, particularly for the dark matter, are remarkably similar in shape, showing little variation in width and are simply scaled in amplitude. The gas distribution becomes more and more peaked for lines with larger N_{HI} , as the thermal pressure that gives rise to the rounded distribution for low-column density lines becomes less important (see also Meiksin 1994). Similarly the central temperature dip and the velocity kink become less pronounced with increasing column density up until

$N_{HI} \sim 10^{14}$. At this point, the peculiar infall velocity actually becomes larger than the Hubble flow and the object has collapsed. Once this happens, two shocks form on either side of the mid-plane and propagate outwards (visible in the velocity distribution at $\pm 10 \text{ km/s}$). If this occurs in a sheet, then the object forms a Zel'dovich pancake (otherwise the shock is cylindrical in the case of a filament or quasi-spherical for a knot). It is interesting to note that this qualitative change in the physical nature of the line occurs at $N_{HI} \sim 10^{14.5} \text{ cm}^{-2}$, which is also where it appears that the carbon abundance (and by plausible extension, all metals) undergoes a drastic change: from $[C/H] \sim -2.0$ above this cutoff, to less than -3.5 below (Lu et al. 1998). Similar results have been found using OVI as a probe (Davé et al. 1998). This behaviour is in broad agreement with that predicted in the simulations of Gnedin & Ostriker (1997), which explicitly include star formation and production of metals.

Finally, we comment on the fact that the density away from the line drops below the cosmic mean, and in fact, the central values of the smallest lines are consistently below this value. This means that most low column density lines are in voids. The size of these regions are smaller than familiar galactic voids and so the name mini-void has been proposed (Zhang et al. 1998).

2.5. Resolving the Jeans length: reionization-driven winds

The thermal pressure becomes more important for smaller lines until it is sufficient to disperse the feature entirely (Bond, Szalay & Silk 1988). As we pointed out earlier, the highest resolution simulations show small scale fluctuations in the velocity and temperature distributions that are mostly absent in the lower resolutions runs. Here, we offer an explanation for that behaviour. In Figures 9, 10, and 11, we plot the density, temperature and projected peculiar velocity along a line-of-sight (with constant comoving length) at redshifts from $z = 7$ to $z = 2$.

At the earliest time, many of the smallest clumps (which are not fully resolved even at this resolution) have collapsed into sharp density spikes. In this model, reionization occurs shortly after $z = 7$ and by $z = 6$, the gas is almost all uniformly at $T = 15,000 \text{ K}$, regardless of density. When this occurs, the smallest objects expand, driving out a wind.

The result can be seen in the density field, as a smoothing of the smallest scales, but it is in the temperature and velocity fields where the changes are the most startling. By $z = 5$, these winds produce small-scale fluctuations

in the velocity, and in the temperature, as the resulting expansions and contractions cause adiabatic cooling and heating. The fluctuations decay at late times, as the gas rearranges itself to new equilibrium configurations.

In detail, this process is not modeled correctly, partially because we do not have the necessary resolution, but also because we have approximated the radiation field as uniform and isotropic. In fact, discrete ionizing sources will produce I-fronts, which will drive a rocket effect, accelerating the cloud in the direction of the radiation, until it is completely ionized and disperses (Shaprio, Raga & Mellema 1998). Still, the net result should be grossly similar unless an object is sufficiently dense that it is optically thick to the ionizing radiation. Such clouds, in order to survive, will have high column densities ($N_{HI} > 10^{18}$) and have been proposed as the source of some Lyman-limit systems (Abel & Mo 1998). However, unless a significant fraction of the mass is tied up in such systems, they will not greatly affect our results.

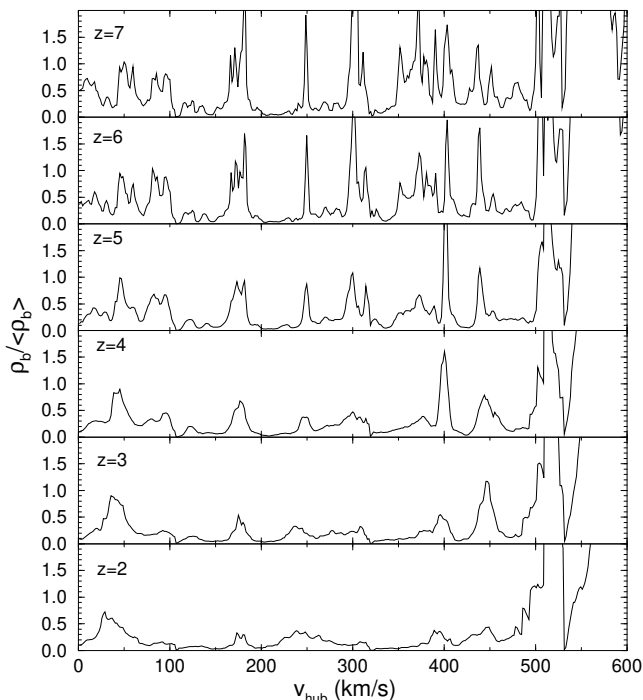


Fig. 9.— The evolution of the baryon overdensity ($\rho_b / \langle \rho_b \rangle$) along a line of sight for the highest resolution simulation (128^3 cells). The ordinate is the Hubble velocity at $z = 2$, with the other redshift ranges adjusted to cover the same comoving length.

2.6. Other statistical measures

The objects that give rise to absorption features in the Lyman-alpha forest are generally not the thermally broadened, compact clouds that the Voigt profile assumes (although it is interesting to note that their mean shape is not so different from a Gaussian). Since this profile is not always a good fit to the observed (or simulated) features, it makes sense to develop other, less parametric ways to characterize the observations. Perhaps the most straightforward is to work directly with the N-point distribution functions of the transmitted flux ($F = e^{-\tau_{HI}}$) itself (Miralda-Escudé et al. 1997; Cen 1997).

In Figure 12, we show the probability distribution from 300 lines-of-sight through the same three simulations previously discussed. The mean flux has been normalized to that found in Zuo & Lu (1993). The two higher-resolution results show very similar distributions, while the lowest exhibits a deficit around $F \sim 0.95$ and a corresponding surplus near $F \sim 0.8$. This follows simply from the profile broadening noticed earlier: narrow lines dip down deeper and so produce lower values of the transmitted flux (higher decrements), leaving more of the spectrum

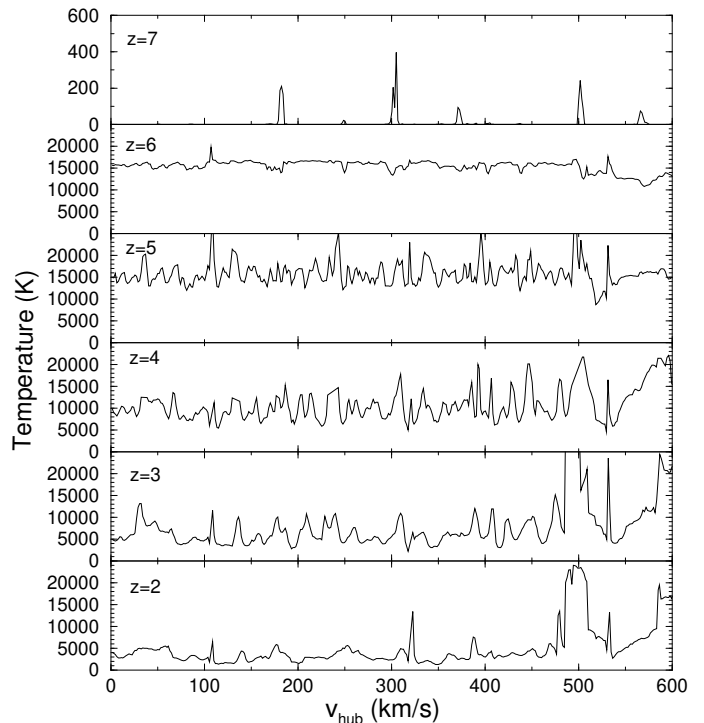


Fig. 10.— The evolution of the baryon temperature along the same line of sight shown in Figure 9.

near its continuum value.

This redistribution of the flux will obviously affect zero-point statistics such as the mean decrement. For example, without renormalizing, the average decrement decreases with resolution: $D_A = 0.229, 0.217, 0.214$ for the 32^3 , 64^3 and 128^3 simulations, respectively. While this is relatively slight, the affect on the He will be even greater (see also Zhang et al. 1998).

A higher order statistic than the flux distribution is the two-point function $P_2(F_1, F_2, \Delta v)$, which gives the probability that two pixels with separation Δv will have flux F_1 and F_2 . In order to present this function graphically, we plot normalized moments of it, averaged over a range of flux (F_a to F_b):

$$\frac{\int_{F_a}^{F_b} dF_1 \int_0^1 dF_2 P_2(F_1, F_2, \Delta v) (F_1 - F_2)}{\int_{F_a}^{F_b} dF_1 \int_0^1 dF_2 P_2(F_1, F_2, \Delta v)} \quad (1)$$

This is the average flux difference as a function of velocity for pixels in the range F_a to F_b , and is plotted in the bottom panel of Figure 12 for three ranges. Although somewhat complicated, it can be interpreted in the following way. For small separations, there is little

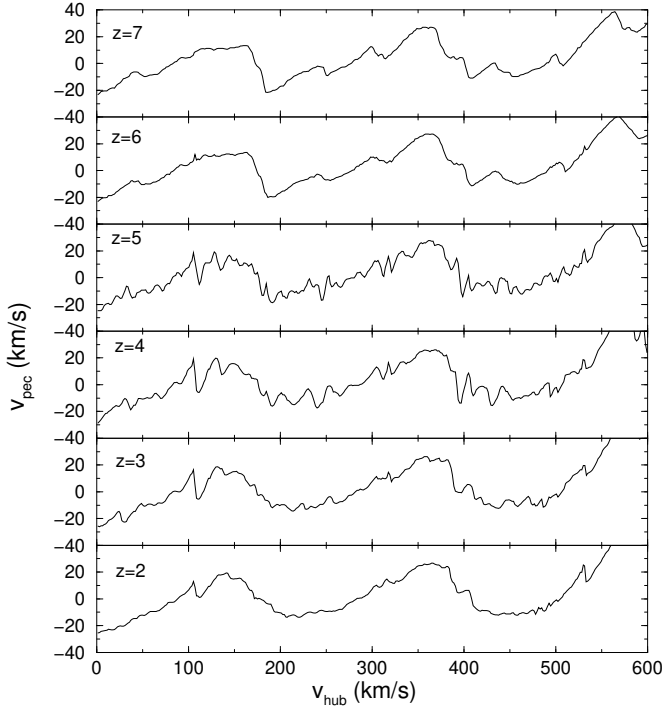


Fig. 11.— The evolution of the projected baryon peculiar velocity along the same line of sight shown in Figure 9.

difference regardless of the flux value, or in other words there is high coherence for small Δv , a fact which is clear from just looking at the spectra. At large separations ($\Delta v > 200$ km/s), there is no coherence, and the value is just the difference between the mean value of the transmitted flux (0.65) and the mean flux in the interval F_a to F_b . For intermediate separations, in the range $\Delta v = 10$ to 100 km/s, the plot shows a measure of the mean profile around pixels with fluxes in that interval (this is heavily influenced by the structure of lines, but around 100 km/s line-line correlations also play a role).

The effect of resolution is again clear, narrowing the line profile as the cell size decreases. Therefore we see that this affect shows up not just in the parametric analysis (Voigt-fitting), but in the distribution of fluxes as well.

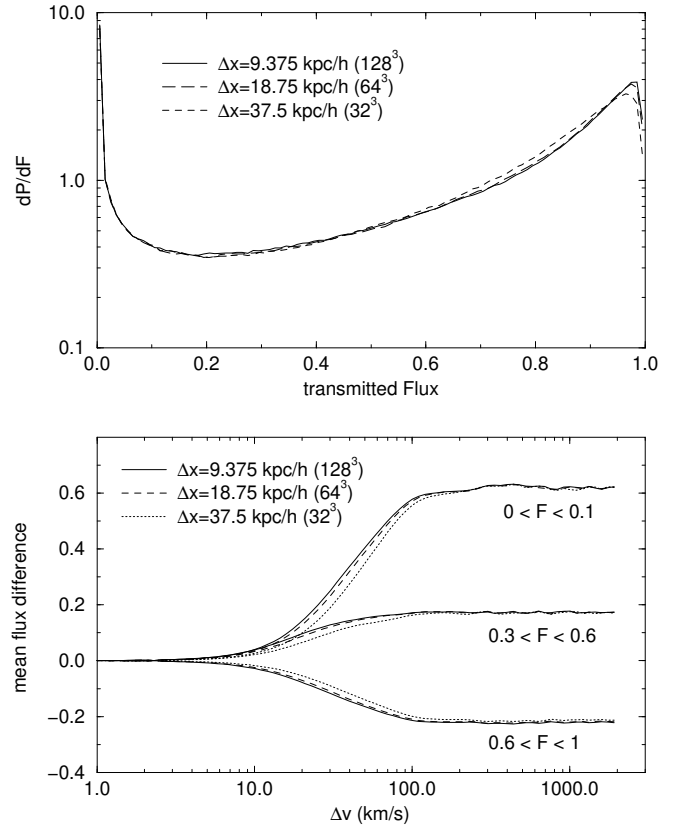


Fig. 12.— The probability distribution (top) of the transmitted flux at $z = 3$ for the same three simulations with different resolutions shown in Figure 3. The bottom panel plots the mean flux difference as a function of velocity difference for pixels in the ranges indicated (eq. 1).

2.7. The effect of large-scale power

In this section, we study the effect of additional large-scale power (see also Wadsley & Bond 1997), both for its own sake, but also to address the question: are the results of the previous discussion biased by the small box size?

In Figure 13, we show density and (volume-weighted) temperature distributions for four simulations with increasing amounts of large-scale power but the same resolution. The smallest box is the same 32^3 simulation analyzed above, while the largest is a 256^3 simulation with a $9.6h^{-1}$ Mpc box size. The distributions are remarkably similar, although there are some differences, particularly for the two smallest boxes.

The biggest difference due solely to the presence of long-wavelength modes is the increased amount of high-temperature gas. As larger modes are included, the bulk velocities increase and the gas that is shock-heated around the edge of the biggest sheets, filaments and knots is correspondingly hotter. If we were looking at the formation of very dense, and hence very rare, clumps (galaxies

and groups), we would also see an increase in the number of these objects; however, their absence has little effect on the low-density regions that occupy most of the volume and hence on the Ly α forest itself. The scatter at high density for the small boxes is simply due to Poisson fluctuations since they have much smaller samples.

The other difference that is apparent is a small shift in the peak temperature, and a slight rearrangement in the low-density end of the baryon distribution (particularly evident in the low ρ_b tail). The evolution of the small boxes is mostly guided by the largest modes in the box, which are not well sampled (i.e. are determined by a small number of random values). They become quasi-linear by $z \sim 3$ and mode-mode coupling starts to play a role, spreading their influence over a wide range of scales. Also, there are no fluctuations above the box size so mode-mode coupling cannot transfer that power down to smaller scales. This means that, on average, there tends to be a deficit of power in small boxes.

Put more simply, these boxes are not fair samples. In fact, if the smaller box sizes ($1.2h^{-1}$ and $2.4h^{-1}$ Mpc) are repeated with a different initial random seed, they show variations of the same magnitude. However, the two larger volumes show nearly identical distributions.

Turning to the observable quantities, we show in Figure 14 the distribution of column densities for these same four simulations, demonstrating again the robustness of this measure. There are, however, some systematic differences, notably for the smallest box which shows a distinct overproduction of moderate to high column density lines. This is again due to the fact that we are not simulating an adequately large volume to contain a reasonable sample, a situation which gets worse at lower redshift as larger regions go non-linear. Although in this case, the result is a flattening of the power-law distribution, we argue that in general either case could occur depending on whether the fluctuations are systematically larger or smaller than average. If we fit power laws to these distributions, the slopes differ by less than 2% for the two largest boxes, but show variations of twice that value for the smaller volumes.

The same effect is operating in the distribution of Doppler b parameters, plotted in Figure 15, causing shifts in the entire distribution for the smaller boxes, while the larger boxes show nearly identical distributions. The magnitude is about 2.5 km/s at $z = 3$.

This is consistent with the fact that scales which give rise to fluctuations on the few hundred kpc scale require box sizes of around $5h^{-1}$ Mpc to resolve properly. For ex-

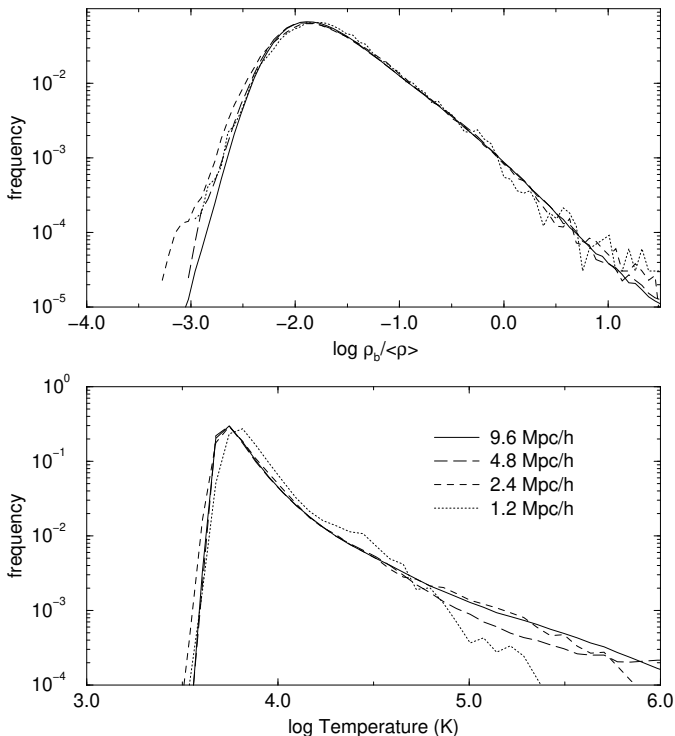


Fig. 13.— The distribution of baryon overdensity (top) and volume-weighted temperature (bottom) for four simulations with increasing box size — but the same resolution — at $z = 3$.

ample, the measure of small scale fluctuations suggested by Gnedin (1998):

$$\sigma_{34}^2 = \int_0^\infty P(k) e^{-2k^2/k_{34}^2} \frac{k^2 dk}{2\pi^2} \quad (2)$$

(where $k = 2\pi/L$, $P(k)$ is the power spectrum at $z = 3$ and $k_{34} = 34\Omega_0^{1/2} h \text{ Mpc}^{-1}$) can be used to make this argument more concrete. If, instead of integrating from 0, we use $k = L/2\pi$ with L the size of the box, and denote this quantity $\sigma_{34}^2(L)$, then the ratio of the power included within the box to the total power: $\sigma_{34}^2(L)/\sigma_{34}^2 = 0.67/0.82/0.92/0.96$ for $L = 1.2/2.4/4.8/9.6 h^{-1} \text{ Mpc}$.

3. Discussion

In the previous section we have shown that while the column density distribution is not a sensitive function of resolution, the Doppler b distribution is, systematically decreasing with resolution. This is important because the median of this distribution was already marginally low for this model, compared to observations. We demonstrated that this is due to intrinsic changes in the den-

sity profile, rather than the temperature or the velocity structure of the lines. The small volumes used to obtain high resolution do cause some change in the median b , but not enough to explain the discrepancy with observations. In this section, we turn first to modeling the effect of resolution and shed some light on the shape of the b -distribution. Then, we briefly discuss ways to reconcile our result with observations.

3.1. Modeling the b -distribution

One of the traditional difficulties in understanding this distribution is the presence of large b values (e.g. Press & Rybicki 1993). To be explained by Doppler broadening, these systems require temperatures too large to be explained by thermal equilibrium. The simulations also produce a large tail, and it is easy to show that there is no correlation between the width of a line and the temperature of the underlying gas. It has recently been pointed out that such a tail is a natural consequence of the filamentary and sheet-like nature of CDM-like structure formation (Rutledge 1998), and the high b -lines arise from oblique lines-of-sight through these structures. To test

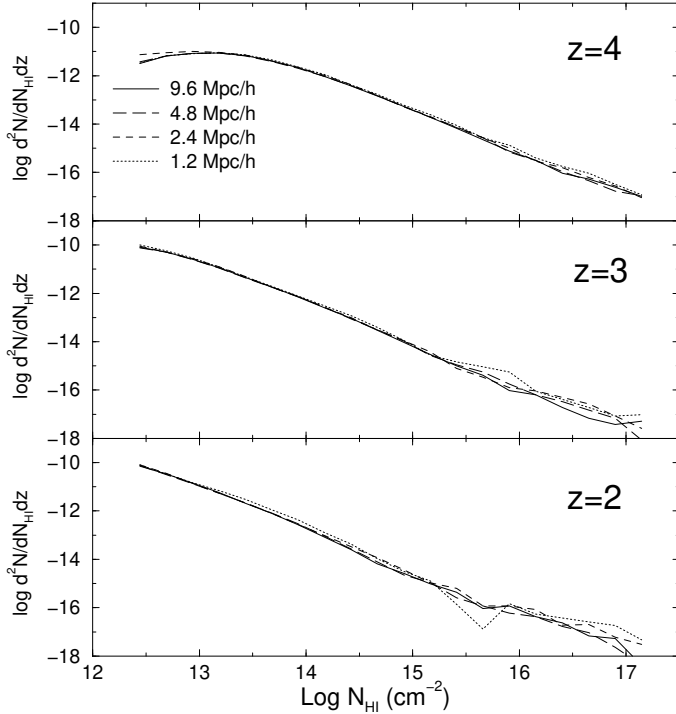


Fig. 14.— The distribution of neutral hydrogen column densities for the same simulations shown in Figure 13, at three different redshifts.

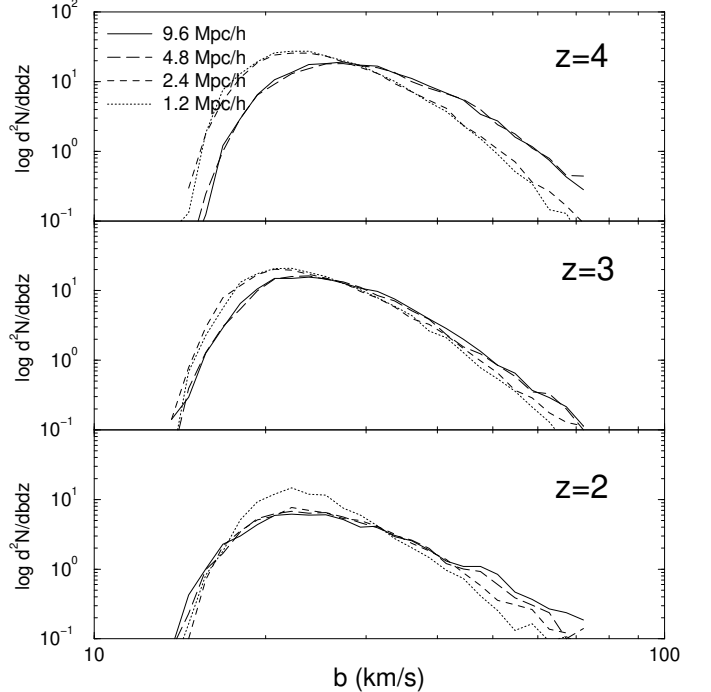


Fig. 15.— The distribution of Doppler b -parameters for the same simulations shown in Figure 13, at three different redshifts.

this idea, we compute, for a large sample of lines, the alignment between the density gradient along the line-of-sight and the line-of-sight vector itself:

$$\cos(\theta) = \sum \frac{|\nabla \rho_b \cdot \mathbf{x}|}{|\nabla \rho_b|}. \quad (3)$$

The sum is over cells that give rise to the line and \mathbf{x} is the line-of-sight unit vector. For sight lines which go perpendicularly through a sheet or filament, the two vectors should line up perfectly and $\cos(\theta) = 1$, while the measure goes to zero as \mathbf{x} becomes parallel to the filament. Figure 16 shows that while there is a lot of noise in the relation, the correlation is clear and goes in the expected direction.

This picture of the clouds also gives us insight into the effect of resolution. It has proved useful to model this, in Eulerian simulations, as a Gaussian smoothing of the density field (Bryan & Norman 1998), with a kernel of approximately two cells. The density profiles of the lines are well modeled by Gaussians, so the typical width should be increased according to:

$$\begin{aligned} b^2(\Delta x) &= b^2(0) + \left(\frac{H(z)2\Delta x}{1+z} \right)^2 \\ &= b^2(0) + H_0^2(2\Delta x)^2(1+z) \end{aligned} \quad (4)$$

where Δx is the comoving cell size at $z = 0$ and $H(z)$ is the redshift-dependent Hubble constant; the second line assumes $\Omega = 1$. The notation $b(0)$ is used to indicate the intrinsic value (i.e. at arbitrarily small cell size).

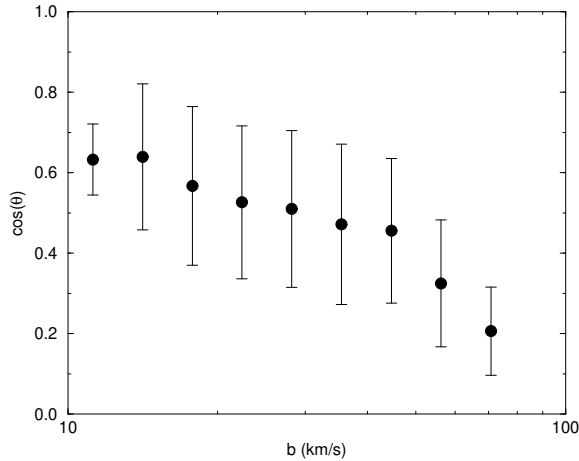


Fig. 16.— The mean alignment of the density gradient and the line-of-sight vector ($\cos(\theta)$) decreases with b . The error bars show the one-sigma variation for each bin.

At this point it is important to recall our model for the lines, particularly those with large b values. If a filament is thickened by smoothing from width l to $(l^2 + (2\Delta x)^2)^{1/2}$, then an oblique line-of-sight through this filament is broadened not by (a term proportional to) Δx added in quadrature, but instead has its b value multiplied by the fraction $(1 + \Delta x^2/l^2)^{1/2}$. The consequence is that, as a reasonable approximation, the entire b distribution should simply scale by a multiplicative factor. (This will be least accurate for low b values where the quadrature addition would be more appropriate).

We test this assertion on the distributions plotted originally in Figure 4. Since they are log-log plots, we can simply shift the curves to the left (and up, since the distribution is per unit b) by the constant factor $f = b_\sigma(0)/b_\sigma(\Delta x)$, where b_σ is a characteristic value which we take to be the median. The result is plotted in Figure 17.

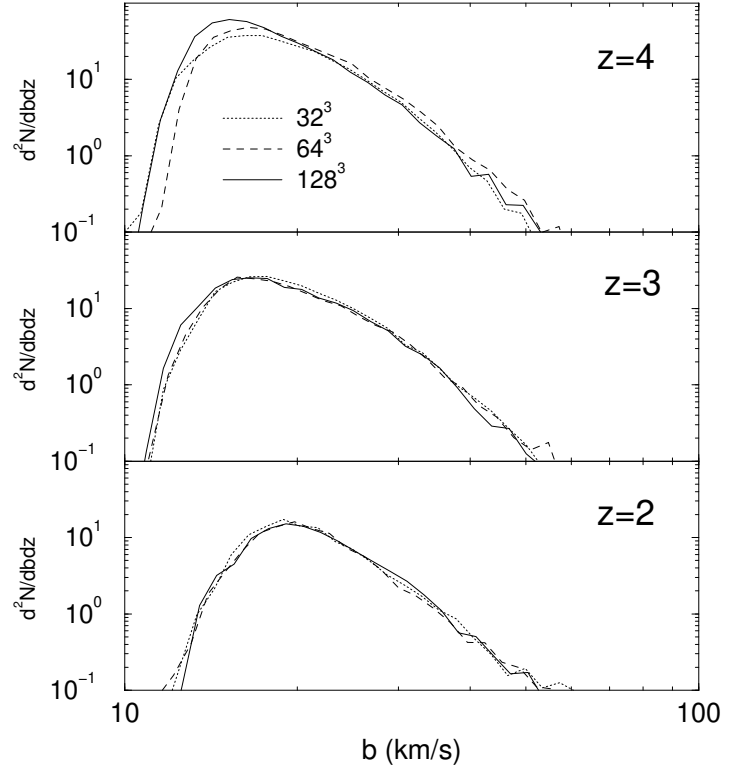


Fig. 17.— The distribution of Doppler b parameters (for lines with column densities $10^{13} < N_{HI} < 10^{14} \text{ cm}^{-2}$) for the same three redshifts and resolutions as in figure 3 (the box size is $1.2h^{-1} \text{ Mpc}$). The distributions have been scaled to account for resolution as described in the text.

This scaling works remarkably well, except for the low b end of the distribution at $z = 4$ (and to a lesser extent at $z = 3$). This is not surprising, given that our approximation breaks down for low b values. Still, it provides a useful way to correct lower resolution simulations: distributions can be scaled as described above and the median (or mean) corrected by equation 4. For example, the median values predicted at $z = 2$ are 21.0, 21.3, 21.4 km/s for the 32^3 , 64^3 and 128^3 simulations. For $z = 3$ these numbers are 19.8, 19.7 and 19.5 km/s, while for the worst case, $z = 4$, they are 18.1, 18.9 and 17.5 km/s.

The ability to do this correction is important since it is very difficult to both get a large enough box and sufficient resolution to reliably calculate this distribution. We make a best estimate for the median of the b distribution in the range $N_{HI} = 10^{13}$ - 10^{14} cm $^{-2}$ by combining two simulations: one (L9.6 from Table 1), our largest simulation, but at a relatively low resolution, and another (L4.8HR) with better resolution, but a somewhat smaller box. The results are shown in Table 2; the remaining differences are most likely due to the large-scale power missing from the smaller box.

3.2. The conflict with observations

To highlight the fact that the predictions of this model for the b -parameter do disagree with observations, we plot both in Figure 18, for $z \sim 2$ and $z \sim 3$. While the shapes are roughly in agreement, the predicted medians are substantially too low, in both cases (the observed median is about 30 km/s). In this same plot, we also show the analytic profile suggested by Hui & Rutledge (1998), based on the Gaussian nature of the underlying density and velocity fields:

$$\frac{dN}{db} \propto \frac{b_\sigma^4}{b^5} \exp \left[-\frac{b_\sigma^4}{b^4} \right]. \quad (5)$$

The normalization and the parameter b_σ have been adjusted to fit the simulations (observations) in the top (bottom) panel, in order to demonstrate the relatively good agreement in shape.

How to restore agreement?

One possible answer is to find a way to increase the temperature of the gas. While this will help by adding to the thermal broadening, it is clear that this will not be sufficient for the large b lines. Another way to see this is, if thermal broadening dominated, then our calculations would predict a correlation between b and N_{HI} , since there is a correlation between T and N_{HI} ; none is seen. Instead, the increased thermal pressure must act to widen the physical structures which give rise to the

lines (this also means that we cannot mimic the effect in the simulations by simply increasing the temperature at the analysis stage). Figure 8 shows that such a process will require high temperatures, particularly for the larger column density lines.

Such a large increase (at least a factor of two) in the temperature seems to be difficult to accomplish. One way is to ionize He around $z \sim 3$, but this only appears to boost the temperature by at most 20% (Hui & Gnedin 1997; Haehnelt & Steinmetz 1997). Delaying reionization also helps because the gas retains some memory of its initial temperature, but even runs with sudden reionization at $z = 5$ doesn't change the b distribution significantly. Similarly, increasing Ω_b boosts the equilibrium temperature, but because $T \sim \Omega_b^{1/1.7}$, even a factor of two change in Ω_b — which conflicts with big-bang nucleosynthesis —

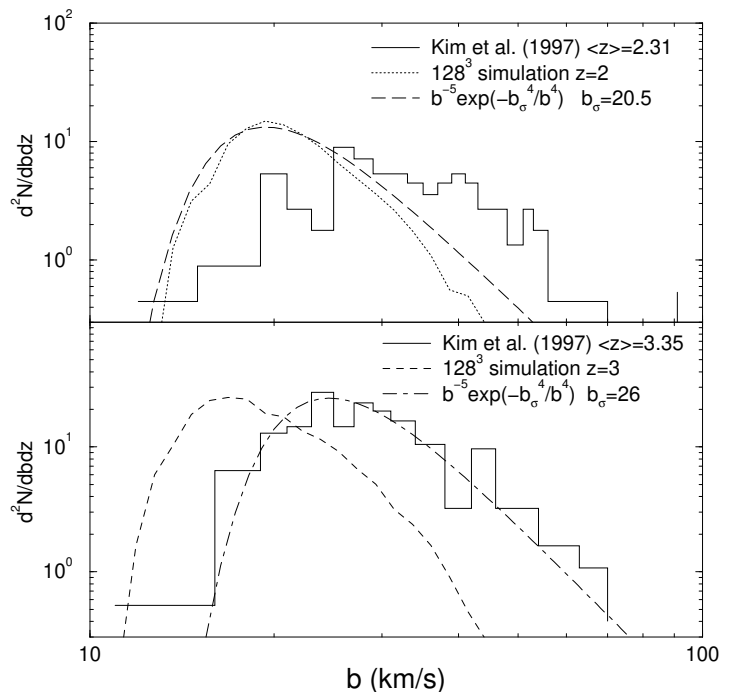


Fig. 18.— The distribution of b parameters for lines with column densities $10^{13} < N_{HI} < 10^{14}$ cm $^{-2}$. The top panel shows observational data (Kim et al. 1997) at a mean redshift of 2.31 as well as the b distribution from our 128^3 simulation at $z = 2$; The dashed line is an analytic profile fit to the simulated data. The bottom panel shows the profile for observational data at $z = 3.35$ and simulated data from $z = 3$. The same analytic profile is now fit to the observations.

TABLE 2
BEST ESTIMATE MEDIAN b -PARAMETER

| simulation | $z = 2$ | $z = 3$ | $z = 4$ |
|------------|---------|---------|---------|
| L9.6 | 24.4 | 21.7 | 22.4 |
| L4.8HR | 22.4 | 19.4 | 20.2 |

only increases the temperature by 50%, which again is not enough. All runs in this paper have included a non-equilibrium chemical model, which increases the temperature slightly over the assumption of equilibrium ionization, but clearly not enough. We have, however, assumed that the radiation field is uniform. This approximation will modify the thermal history somewhat, but seems unlikely to have a large effect (Meiksin 1994; Miralda-Escudé & Rees 1994; Giroux & Shapiro 1996).

One last way to increase the gas temperature is to use thermal energy from star formation which, of course, we do not include in the simulations. This is difficult to rule out, but the low metallicity of the low column density gas seems to argue against it (Davé et al. 1998; Giroux & Shapiro 1996).

Instead, a more natural way is to change the density distribution directly, through the power spectrum or cosmology. We have only examined the standard cold dark matter model, and it is possible that other models will be more successful. We address this topic in a future paper.

This work is done under the auspices of the Grand Challenge Cosmology Consortium and supported in part by NSF grants ASC-9318185 and NASA Astrophysics Theory Program grant NAG5-3923. MLN acknowledges useful conversations with Martin Haehnelt. MLN and GB thank Tom Abel for his help.

REFERENCES

- Abel, T., Anninos, P., Zhang, Y., Norman, M.L., 1997, *New Astronomy*, 2, 181
- Abel, T. & Mo, H.J. 1998, *ApJ*, 494, L151
- Anninos, P., Zhang Y., Abel, T., Norman, M.L., 1997, *New Astronomy*, 2, 209
- Bi, H.G. 1993, *ApJ*, 405, 479
- Bi, H.G. & Davidsen, A. 1997, *ApJ*, 479, 523
- Bond, J.R., Szalay, A.S. & Silk, J. 1988, *ApJ*, 324, 627
- Bond, J.R. & Wadsley, J.W. 1997, to appear in *Proceedings of the 13th IAP Colloquium, Structure and Evolution of the Intergalactic Medium from QSO Absorption Line Systems*, eds. P. Petitjean & S. Charlot (Nouvelles Frontières: Paris)
- Bryan, G.L., Norman, M.L., Stone, J.M., Cen, R., Ostriker, J.P. 1995, *Comput. Phys. Comm.*, 89, 149
- Bryan, G.L. & Norman, M.L. 1998, *ApJ*, 495, 80
- Cen, R., Miralda-Escudé, J., Ostriker, J.P., Rauch, M. 1994, *ApJ*, 437
- Cen, R. 1997, *ApJ*, 479, L85
- Cen, R. & Simcoe, R.A. 1997, *ApJ*, 483, 8
- Croft, R.A.C., Weinberg, D.H., Katz, N., Hernquist, L. 1998, *ApJ*, 495, 44
- Davé, R., Hernquist, L., Weinberg, D.H. Katz, N. 1997, *ApJ*, 477, 21
- Davé, R., Hellsten, U., Hernquist, L. Katz, N. & Weinberg, D.H. 1998, *ApJ*, submitted (astro-ph/9803257)
- Giroux, M.L. & Shapiro, P.R. 1996, *ApJS*, 102, 191
- Gndein, N.Y. 1998, *MNRAS*, submitted (astro-ph/9706286)
- Gnedin, N.Y. & Hui, L.. 1998, *MNRAS*, 296, 44
- Gnedin, N.Y. & Ostriker, J.P. 1997, *ApJ* 486, 581
- Haehnelt, M.G. & Steinmetz, M. 1997, *MNRAS*, submitted (astro-ph/9706296).
- Haardt, F. & Madau, P. 1996, *ApJ*, 461, 20
- Hernquist, L., Katz, N., Weinberg, D.H., Miralda-Escudé, J. 1996, *ApJ*, 457, 51L
- Hu, E., Kim, T.-S., Cowie, L.L., Songaila, A., & Rauch, M. 1995, *AJ*, 110, 1526
- Hui, L., Gnedin, N.Y. & Zhang, Y. 1997, *ApJ*, 486, 599
- Hui, L. & Gnedin, N.Y. 1997, *MNRAS*, 292, 27
- Hui, L. & Rutledge, R.E. 1998, preprint (astro-ph/9709100)
- Kim, T.-S., Hu, E.M., Cowie, L.L. & Songaila, A. 1997, *AJ*, 114, 1
- Kirkman, D. & Tytler, D. 1997, *ApJ*, 484, 672
- Lu, L. Sargent, W.L.W., Barlow, T.A. & Rauch, M. 1998, preprint (astro-ph/9802189).
- Machacek et al. 1998, in preparation
- Meiksin, A. 1994, *ApJ*, 431, 109
- Meiksin, A. & Madau, P. 1993, *ApJ* 412, 34
- Miralda-Escudé, J. & Rees, M.J. 1994, *MNRAS*, 266, 343
- Miralda-Escudé, J., Renyue, C., Ostriker, J.P., Rauch, M. 1997, *ApJ*, 471, 582
- Miralda-Escudé, J., Rauch, M., Sargent, W.L.W., Barlow, T.A., Weinberg, D.H., Hernquist, L., Katz, N., Cen, R., Ostriker, J.P. 1997, To appear in *Proceedings of 13th IAP Colloquium: Structure and Evolution of the IGM from QSO Absorption Line Systems*, eds. P. Petitjean, S. Charlot
- Press, W.H., Rybicki, G.B., Schneider, D.P. 1993, *ApJ*, 414, 64
- Press, W.H. & Rybiki, G.B. 1993, *ApJ* 418, 585
- Rauch, M., Miralda-Escudé, J., Sargent, W.L.W., Barlow, T.A., Weinberg, D.H., Hernquist, L., Katz, N., Cen, R., Ostriker, J.P. 1997, *ApJ*, 489, 7
- Rutledge, R.E. 1998, *ApJ*, submitted (astro-ph/9707334)
- Shapiro, P., Raga, A.C. & Mellema, G. 1998, To appear in *Proceedings of the Workshop on H_2 in the Early Universe*, eds. F. Palla, E. Corbelli, and D. Galli, *Memorie Della Societa Astronomica Italiana*, in press
- Theuns, T., Leonard, A., Efstathiou, G., Pearce, F.R. and Thomas, P.A. 1998, astro-ph/9805119.

- Weinberg, D.H., Hernquist, L., Katz, N., Croft, R., Miralda-Escudé, J. 1997, to appear in Proceedings of the 13th IAP Colloquium, Structure and Evolution of the Intergalactic Medium from QSO Absorption Line Systems, eds. P. Petijean & S. Charlot (Nouvelles Frontières: Paris)
- Viana, P.T.P. & Liddle, A.R. 1996, MNRAS, 281, 323
- Wadsley, J.W. & Bond, J.R. 1997, in Computational Astrophysics, Proc. 12th Kingston Conference, Halifax, Oct. 1996, ed. D. Clarke & M. West (PASP), p. 332
- White, S.D.M., Efstathiou, G., Frenk, C.S. 1993, MNRAS, 262, 1023
- Zhang, Y., Anninos, P., Norman, M.L. 1995, ApJ, 453, L57
- Zhang, Y., Anninos, P., Norman, M.L., Meiksin, A. 1997, ApJ, 485, 496
- Zhang, Y., Meiksin, A., Anninos, P., Norman, M.L. 1998, ApJ, 495, 63
- Zuo, L. & Lu, L. 1993, ApJ, 418, 601